Determination of Local Fine Structure of Blood Flows by Measurement Coupled Simulation

Toshiyuki Hayase

Professor
Transdisciplinary Fluid Integration Research Center, Institute of Fluid Science
E-mail: hayase@ifs.tohoku.ac.jp

1. Introduction

Understanding complex blood flows in living bodies is essential to realize advanced diagnosis and treatment for circulatory diseases. The author's group is doing research to analyze complex blood flows by numerical simulation, experimental measurement, and their coupled method in order to determine the local and fine structure of complex blood flows.

This article explains recent research activities of our research group on the measurement coupled simulation of blood flows [1] and the cellular flow in microcirculation [2].

2. Measurement Coupled Simulation of Blood Flows

2.1. Introduction

Hemodynamic stresses such as wall shear stress and pressure affect the endothelial cells on blood vessels, resulting in changes of their mechanical properties [3,4]. These changes can cause a blood vessel to degenerate, eventually leading to circulatory diseases. An aneurysm is a pathological circulatory condition in which the blood vessel expands like a balloon, the rupture of which may be fatal. Although many researchers have reported that the development, progress and rupture of aneurysms are related to the hemodynamics, the existing diagnosis of aneurysms mainly considers the anatomical abnormalities shown by X-ray CT, MRI or ultrasonography. These include the maximum diameter and growth rate for thoracic and abdominal fusiform aneurysms [5] and the aspect ratio for cerebral saccular aneurysms as empirical indications of aneurysmal rupture. For a saccular aneurysm of the thoracic aorta, which is dealt with in this study, the size (larger than 5 cm) and the expansion rate (faster than 5 mm per a year) are used as the criteria for surgery. Those criteria are still limited since there are numerous cases of ruptures of aneurysms which are judged to be unlikely to rupture. Therefore, an advanced diagnosis for optimum treatment of aneurysms, including surgery, must be made with reference to accurate and detailed information on the blood flow field of each patient.

Figure 1 shows a block diagram of the UMI simulation. In this simulation, feedback signals are generated proportional to the difference between the Doppler velocities obtained by ultrasonic measurement and computation, and are added to the numerical simulation as an artificial force at a number of grid points selected as the feedback points in the feedback domain during the computational process. In a former study [6], we proposed feedback formulae of the UMI simulation and confirmed their efficiency for a two-dimensional blood flow field in a descending aorta with an aneurysm. The effect of the arrangement of the feedback points and the feedback domain was systematically investigated to reveal detailed particulars of the UMI simulation by the same two-dimensional numerical experiment [7]. For practical use of the UMI simulation in medical procedures, extended investigation of the efficiency of the UMI simulation for the blood flow field in realistic three-dimensional geometry is essential. In addition, as the transient characteristics of the UMI simulation determine the convergence to the target flow as well as the frequency response to the oscillatory blood flow, it is critically important that they be clarified.

This study concerns the transient and steady characteristics of the UMI simulation by evaluating convergence of the solution for the three-dimensional steady blood flow with the average inlet velocity as the mean value over one cardiac cycle. We did not use real ultrasonic measurement for the reference data since although it provides the information necessary for the feedback in the UMI simulation, i.e., Doppler velocity, it does not provide other information necessary for evaluating the UMI simulation such as three-dimensional velocity vectors or pressure field. Rather, we used a numerical solution as a model of real blood flow in order to perform numerical experiment. A steady standard numerical solution with realistic boundary conditions was first defined, and then UMI simulations were carried out with incorrect boundary

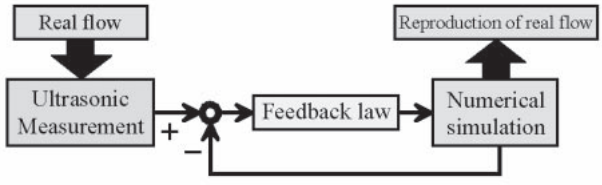

Fig. 1. Schematic diagram of UMI simulation.

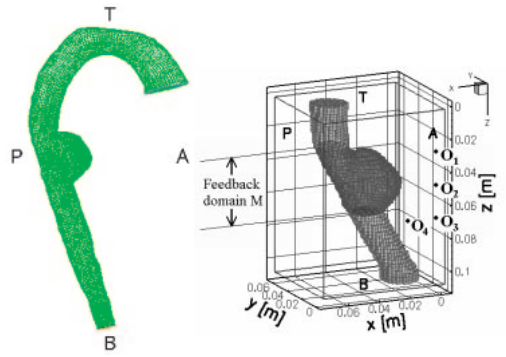

(a) (b)

Fig. 2. Computational domains of (a) whole aorta with an aneurysm for FLUENT and of (b) blood vessel in the vicinity of a thoracic aneurysm with feedback domain M and four origins of ultrasonic beam or probe positions for UMI simulation.

conditions but applying feedback signals in an aneurysmal domain with various feedback arrangements. The transient and steady characteristics of the UMI simulation were evaluated for a variety of feedback gains with one ultrasound probe by changing the location, or with two or three probes at fixed positions.

2.2. Methods

In this section, numerical experiment procedure is first explained, and UMI simulation for a thoracic aneurysm is formulated. Then, the settings of numerical experiment to investigate the transient and steady characteristics of the UMI simulation is explained in detail.

Numerical experiment procedure

We focused on the blood flow in an aorta with an aneurysm, namely, that of a 76-year-old female patient with a chronic aortic aneurysm in her descending aorta. She had no significant cardiac complications. The cardiac output was 7.0×10^{-5} m^3s^{-1} (4.2 $l\cdot min^{-1}$) and the heart rate was 1.0 Hz (61 bpm) during the measurement. Figure 2(a) shows the full blood vessel configuration reconstructed from the sliced images acquired by X-ray CT (AquilionTM 16, Toshiba, Tokyo, Japan). The UMI simulation in this study dealt with the blood flow in a partial domain in the vicinity of the aneurysm as shown in Fig. 2(b). The z-axis was defined along the body axis direction, and the x and y-axes were anterior-posterior and right-left directions, respectively. The aneurysm was located in the range of 0.028 m $\le z \le$ 0.068 m in Fig. 2(b). All measurement data were obtained at Tohoku University Hospital.

We first performed the numerical simulation of blood flow in the full domain shown in Fig. 2(a), applying a parallel flow with a uniform velocity profile as the upstream boundary. We then obtained a model of the real blood flow, or the standard solution, as the computational result in the partial domain shown in Fig. 2(b) by specifying the upstream and downstream boundary conditions obtained from the former simulation with the full vessel configuration.

Table 1. Computational condition.

Entrance vessel diameter D	23.47×10^{-3} m
Kinematic viscosity ν	4.00×10^{-6} m^2/s
Inlet average velocity u'_{in}	2.00×10^{-1} m/s
Characteristic time D/u'_{in}	1.17×10^{-1} s

In UMI simulation, we assume that the velocity profiles at the upstream and downstream boundaries in the computational domain of Fig. 2(b) are unknown, and specify the parallel flow with a uniform velocity profile at the upstream boundary and free flow condition at the downstream boundary. These inaccurate boundary conditions cause error as compared with the model of the real blood flow. The UMI simulation here performed was intended to reduce the error in the aneurysm by feeding back the signals to compensate for the errors of the Doppler velocities in the numerical simulation. Since the computational result converges to the target flow with the aid of the feedback process in the UMI simulation, unsteady flow computation is required for the UMI simulation even for the present steady target flow.

The variation of computational accuracy for the sake of feedback was evaluated by comparing the result of UMI simulation with the standard solution and the result of ordinary numerical simulation in which no feedback signal was applied.

Governing equations

Blood is assumed to be a Newtonian fluid with a density $\rho = 1.00\times10^3$ $kg\cdot m^{-3}$ and a dynamic viscosity $\mu = 4.00\times10^{-3}$ Pa·s within normal range. Governing equations are the Navier-Stokes equations for incompressible and viscous fluid flow,

$$\rho\left(\frac{\partial \mathbf{u}}{\partial t}+(\mathbf{u}\cdot\nabla)\mathbf{u}\right)=\mu\Delta\mathbf{u}-\nabla p+\mathbf{f}, \qquad (1)$$

and the pressure equation

$$\Delta p=-\nabla\cdot\rho(\mathbf{u}\cdot\nabla)\mathbf{u}+\nabla\cdot\mathbf{f}, \qquad (2)$$

where $\mathbf{u} = (u, v, w)$ is the velocity vector, p is the pressure, and $\mathbf{f} = (f_x, f_y, f_z)$ denotes the body force (feedback signal). The pressure equation is derived by substituting the equation of continuity into the divergence of the Navier-Stokes equation, Eq. (1). All the values are nondimensionalized with the characteristic length L of the equivalent diameter of the blood vessel D at the upstream boundary calculated by averaging x-directional and y-directional maximum

lengths of the cross section of the blood vessel at the upstream boundary, the kinematic viscosity ν of the blood, and the characteristic velocity U of the average velocity u'_{in} of the blood at the upstream boundary. The values of the parameters are summarized in Table 1. From here on, the same symbols are used for both dimensional and nondimensional values since it does not cause confusion.

The computational grid shown in Fig. 2(b) was generated by introducing a staggered grid system, in which nodes for velocity components are shifted by half the grid size from the pressure node, with 40×34×49 grid points in x, y and z directions. The grid interval dz in the z-direction was set at 2.00×10^{-3} m (0.0852 in nondimensional value), which was the same as the slice interval of the X-ray CT, and those in the other directions were determined to be $dx = dy = 1.78\times10^{-3}$ m (0.0758 in nondimensional value), compromising reproducibility of vessel configuration and computational load.

The governing equations were discretized by means of the finite volume method and were solved with an algorithm similar to the SIMPLER method [8]. The convective terms were discretized with the reformulated QUICK scheme [9]. The time derivative terms were discretized with the first order Euler implicit scheme. Linear algebraic equations were solved using the MSI scheme.

Feedback law

The feedback signal applied at a feedback point is an artificial body force proportional to the difference between Doppler velocities V_s by ultrasonic measurement and V_c by the UMI simulation as described below:

$$\mathbf{f} = -K_v^* \frac{\mathbf{\Phi}_d(\mathbf{u}_c - \mathbf{u}_s)}{U}\left(\frac{\rho U^2}{L}\right), \quad = -K_v^* \frac{\mathbf{\Phi}_d(\mathbf{u}_e)}{U}\left(\frac{\rho U^2}{L}\right) \tag{3}$$

where K_v^* is the feedback gain (nondimensional), U is the characteristic velocity, L is the characteristic length. $\mathbf{u}_c$ and $\mathbf{u}_s$ are velocity vectors of the computational result and the standard solution (or real flow), respectively, $\mathbf{u}_e$ is the error velocity vector, and $\mathbf{\Phi}_d$ (d = 1, 2, 3) is a projection function of a three-dimensional vector to the d-dimensional subspace generated by the vectors of the ultrasonic beam directions.

For the diagnostic measurement of the blood flow field in an aneurysm which develops in the descending aorta, transesophageal ultrasonography is carried out. This method irradiates and receives ultrasound using an ultrasound probe located inside the esophagus and provides Doppler velocities and a cross-sectional B-mode image of the blood vessel. In the UMI simulation, in order to make the computational result converge to the real flow, feedback signals are generated by comparing the computed Doppler velocities with the corresponding ultrasonic measurement data and are fed back to the numerical simulation to compensate for the error. For the feedback in the UMI simulation, the feedback domain is arranged in the computational domain, and then the

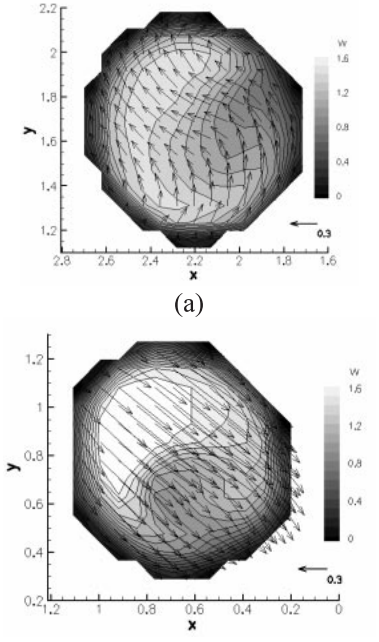

Fig. 3. Velocity profiles at (a) upstream and (b) downstream boundaries for the standard solution (nondimensional).

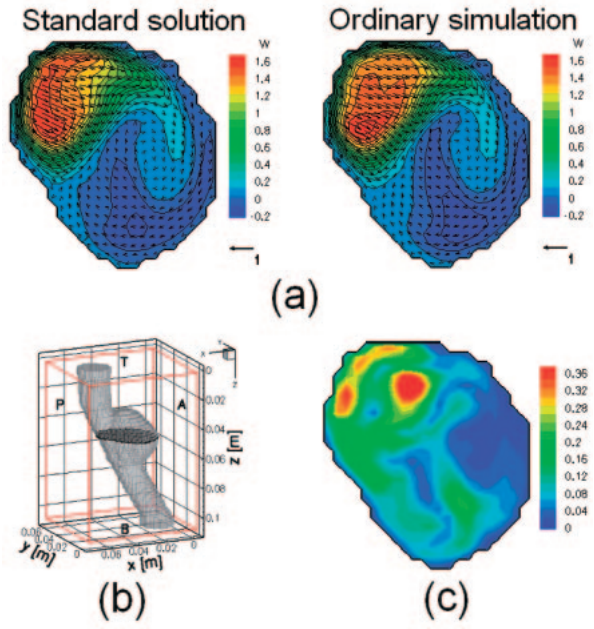

Fig. 4. (a) Velocity distribution of standard solution and ordinary simulation. (b) cross section of aneurysm at z = 0.048 m, and (c) error norm distribution of velocity vector of the ordinary simulation.

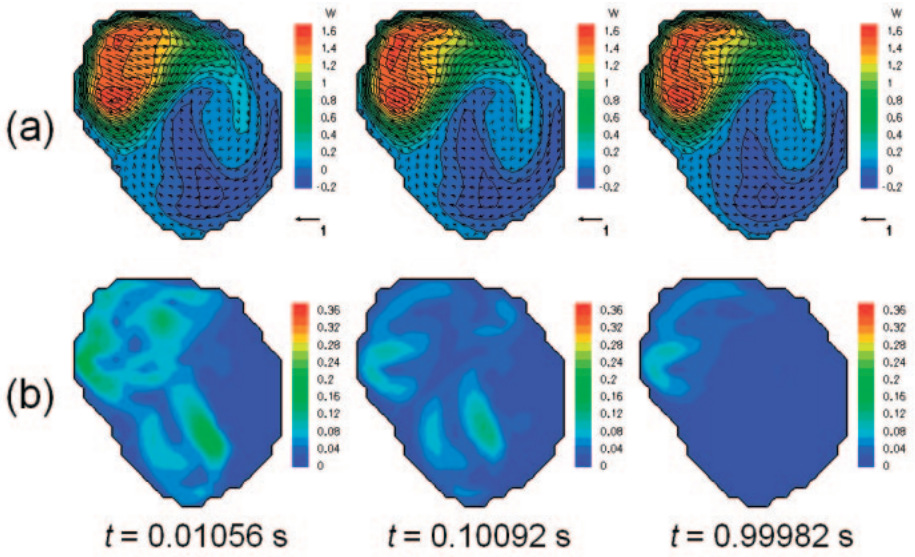

Fig. 5. Time-variation of (a) axial velocity contour and transverse velocity vectors and (b) distribution of error norm of velocity vector in the UMI simulation using one ultrasound probe at O2 at Kv* = 160.

grid points in the fluid region in the feedback domain are chosen as the feedback points at which feedback signals are generated and added to the computational model. In this study, we determined the feedback domain M which covered the whole aneurysm as colored with dark gray in Fig. 2(b). The feedback points were defined at all grid points (6002 points in total) in the feedback domain M referring to the former study [7]. This is the ideal situation, but it has been revealed that the computational accuracy of UMI simulation is little sensitive to the reduction of feedback point density in some extent. Especially, the acquisition of Doppler velocity data on multiple transverse cross sections of blood vessel leads better reproduction of flow field than that on longitudinal cross sections due to the effect of flow convection.

Initial and boundary conditions on subdomain

Concerning the boundary conditions, we assumed a parallel flow with a uniform velocity profile at the upstream boundary and the free flow condition ($\partial/\partial n$ = 0, n: coordinate normal to the boundary) at the downstream boundary for the UMI simulation and the corresponding ordinary simulation since the exact velocity profiles are usually unknown in practice. For the standard solution, we specified the velocity vector distributions at the upstream and downstream boundaries as mentioned below. In each numerical simulation, the no-slip condition was applied to the blood vessel wall. As to the initial condition, the UMI simulation was started from the steady solution of the ordinary numerical simulation without feedback.

Velocity profiles at the upstream and downstream boundaries specified for the standard solution or the model of real blood flow to be reproduced by UMI simulation are shown in Fig. 3. Those velocity profiles were obtained from the preliminary simulation using commercial computational fluid dynamics software (FLUENT 6.1.22, Fluent Inc., Lebanon, NH, USA) with a full configuration of the aorta, which included the blood vessel as shown in Fig. 2(a). In the computation using FLUENT, we applied steady uniform velocity at the inlet of the ascending aorta.

2.3. Results

Computational results are basically presented in nondimensional value. However, some values such as time are presented in dimensional value to get insight for practical applications.

Figure 4(a) compares the velocity profiles, displayed with contours of the axial velocity component and vectors of the transverse velocity components, between the standard solution and the steady state ordinary simulation on the middle cross section of the aneurysm at z = 0.048 m (see Fig. 4(b)), and Fig. 4(c) shows the distribution of the error norm $e_n(\mathbf{u}, t_\infty)$ of the velocity vector for the above ordinary simulation in steady state at $t = t_\infty = 1.17\times10^9$ s (1.0×10^{10} in nondimensional value). Though the velocity profile obtained by the ordinary simulation is qualitatively the same as that of the standard solution, relatively large errors of more than 0.2 occurred in the parent artery and inside the aneurysm as observed in Fig. 4(c) due to the inaccurate boundary conditions of the ordinary simulation.

Corresponding results of the UMI simulation using one ultrasound probe at O_2, time-variations of the velocity profile and the error distribution $e_n(\mathbf{u}, t)$ are shown in Fig. 5. The initial condition of the UMI simulation at t = 0 s corresponds to the steady state ordinary simulation in Fig. 4. As observed in Fig. 5(a),

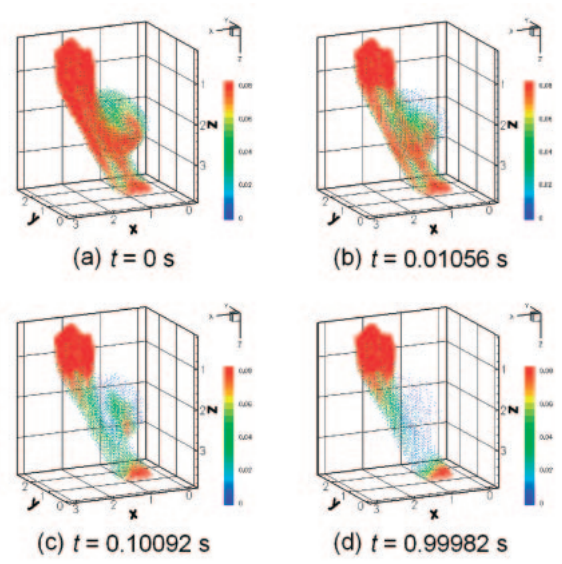

Fig. 6. Time-variation of velocity error vectors in the vicinity of an aneurysm in the UMI simulation using one ultrasound probe at O2 at Kv* = 160 (nondimensional)

starting from the result of the ordinary simulation (right portion of Fig. 4(a)), the velocity profile of the UMI simulation gradually approaches the standard solution (left portion of Fig. 4(a)). As a result, in Fig 5(b), the error norm is reduced and the large errors observed in the result of the ordinary simulation disappear at t = 0.99982 s (8.52 in nondimensional value) (maximum error is 9.59×10^{-2}).

For a more global observation of the effect of the feedback, time variation of the velocity error vectors against the standard solution is shown in Fig. 6. In the initial state at t = 0 s, the result is the same as that of the ordinary simulation without feedback, and large error vectors (colored with red) resulting from inaccurate boundary conditions exist (see Fig. 6(a)). With time, the error vectors decrease in and after the feedback domain due to the effect of the feedback in the UMI simulation and converge to the steady state of the velocity error vectors (see Fig. 6(d)).

2.4. Discussion

The error vectors in the ordinary simulation are significant at some distance from the upstream boundary and in the small region near the downstream boundary, and they are still exist but are somewhat reduced in the aneurysm because of decreased velocity (Figs. 6(a)). In the convergent steady state of the UMI simulations (Figs. 6(d)), the magnitudes of the error vectors in the aneurysm are significantly reduced in comparison with those in the ordinary simulation. In contrast, relatively large error vectors remain near the upstream and downstream boundaries because of the inaccurate boundary conditions. More error vectors are

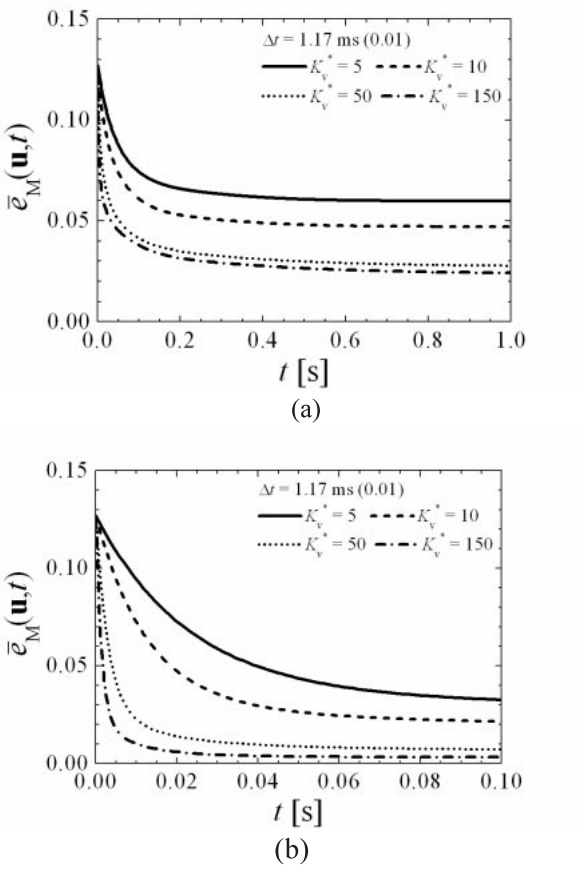

Fig. 7. Reduction of average error norm of velocity vector in the feedback domain M of the UMI simulations using (a) one probe at O2 or (b) two probes at O1 and O3 with various feedback gains

observed in the upstream region of the feedback domain than in the downstream region. These results suggest that the improvement of the computational accuracy downstream of the feedback domain occurs to some extent because of flow convection.

At each time step, the error against the standard solution in the feedback domain was evaluated by the average error norm $\bar{e}_M(\mathbf{u}, t)$ of the velocity vector in the feedback domain M. Figure 7 shows variations of $\bar{e}_{\square}(\mathbf{u}, t)$ of the UMI simulation using one probe at O_2 (Fig. 7(a)) and two probes at O_1 and O_3 (Fig. 7(b)) at four feedback gains, respectively. Note that the time scale in Fig. 7(b) is ten times smaller than that in Fig. 7(a). The initial value is the error of the ordinary simulation. Each error norm in Fig. 7(a) decreases and converges to each constant value. Increasing the feedback gain K_v^* causes the error to decrease faster and the steady error to become smaller. Further increase of feedback gain destabilizes the UMI simulation and the error increases above its initial value. The critical feedback gain of divergence was 170. The UMI simulations with two probes in Fig. 7(b) demonstrate more effective performance than that with one probe. The convergence of the UMI simulation is accelerated by using two probes. Moreover, steady error of the UMI

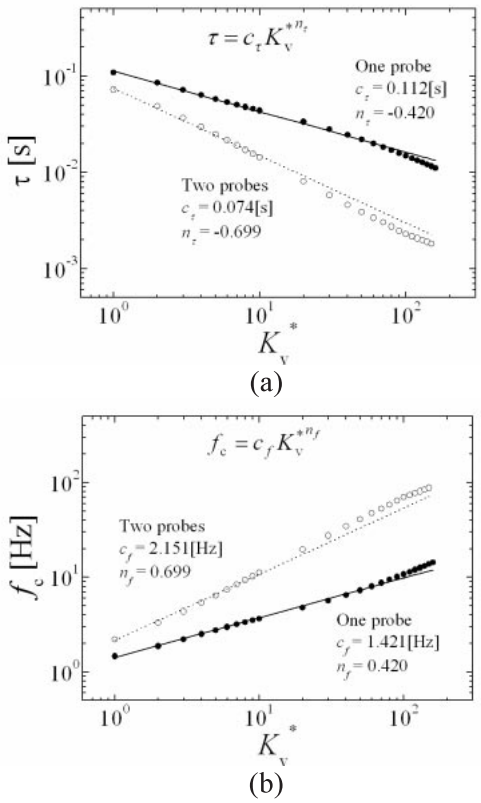

Fig. 8. (a) Time constant and (b) cutoff frequency of the UMI simulations using one probe at O2 or using two probes at O1 and O3 as a function of feedback gain.

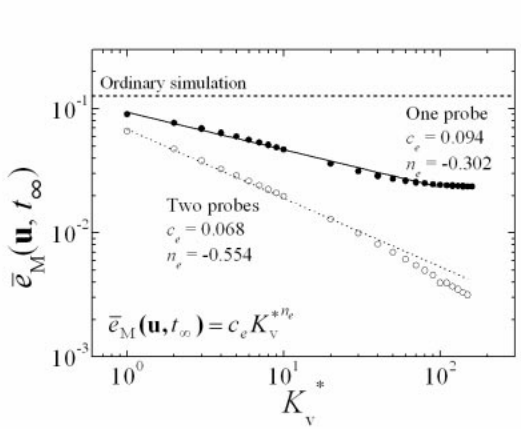

Fig. 9. Variation of average error norm of velocity vector of UMI simulations using one probe at O2 or two probes at O1 and O

simulation using two probes is far smaller than that of the UMI simulation using one probe, especially at large feedback gains. The critical feedback gain of divergence for two probes was 160.

Transient and steady characteristics of UMI simulation are discussed in the following. The transient response of the UMI simulation is evaluated by the time constant τ [s] and the resultant cutoff frequency f_c [Hz]. Referring to the definition of the time constant of the first order lag element, we define the time constant τ as the time in which the average error norm $\bar{e}_M(\mathbf{u}, t)$ of velocity vector in the feedback domain is reduced e^{-1} (= 0.63) times the total error reduction (e_0-e_s) (e_0: initial error, e_s: steady error). The cutoff frequency f_c [Hz] is calculated as $(2\pi\tau)^{-1}$.

Figure 8 shows the time constant τ and the cutoff frequency f_c of the UMI simulation using one probe at O_2 or two probes at O_1 and O_3. In Fig. 8(a), the time constant of the UMI simulations with one probe and two probes is approximated as

$$\begin{aligned} &\tau = c_\tau K_v^{*n_\tau} \\ &\text{One probe}: c_\tau = 0.112[\text{s}], n_\tau = -0.420 \\ &\text{Two probes}: c_\tau = 0.074[\text{s}], n_\tau = -0.699 \end{aligned} \quad . \tag{4}$$

Especially at large feedback gains, the time constant using two probes becomes almost one tenth the value of that when one probe is used.

In Fig. 8 (b), the cutoff frequency of the UMI simulations is approximated from the above results as

$$\begin{aligned} &f_c = c_f K_v^{*n_f} \\ &\text{One probe}: c_f = 1.421[\text{Hz}], n_f = 0.420 \\ &\text{Two probes}: c_f = 2.151[\text{Hz}], n_f = 0.699 \end{aligned} \quad . \tag{5}$$

As observed in the previous section, UMI simulations of the steady flow reduce the error against the standard solution and converge to each steady state of the flow field. The convergent results of the UMI simulations were evaluated using the average error norm $\bar{e}_M(\mathbf{u}, t_\infty)$ of the velocity vector in the feedback domain M at the time for convergence $t = t_\infty$. Figure 9 shows the variations of $\bar{e}_M(\mathbf{u}, t_\infty)$ of the UMI simulations using one probe at O_2 and two probes at O_1 and O_3 with the feedback gain K_v^*. All results of the UMI simulations show lower error than the ordinary simulation, the result of which is shown by the horizontal dashed line in Fig. 9. The error of the UMI simulation using one probe decreased to the -0.302th power of the feedback gain. Note that the reduction rate decreases with increasing K_v^* and the error is almost constant for $K_v^* \geq 100$. This might be ascribed to the instability of the UMI simulation. The UMI simulations using two probes reduced the error to the -0.554th power of the feedback gain, achieving greater reduction than in the case using one probe. In UMI simulations, larger feedback gain is generally preferable for the steady characteristics of small steady state error as well as for the transient characteristics of the small time constant as long as the computation remains stable. The increase of the feedback gain is limited to $K_v^* \leq 160$ for the preset computational time increment $\Delta t = 1.17\times10^{-3}$ s as mentioned above.

2.5. Conclusions

In this study, a numerical experiment of Ultrasonic-Measurement-Integrated (UMI) simulation with inaccurate boundary conditions was performed to reproduce a steady standard solution of the three-dimensional blood flow in an aneurysmal aorta with realistic boundary conditions. The transient characteristics of the UMI simulation were evaluated by the time constant which determines the time necessary for convergence or equivalently the frequency response to the oscillating flow, and the steady characteristics were evaluated by the steady state error of the velocity vectors in an aneurysm.

3. Cellular Flow in Microcirculation

As a fundamental research for modeling of microcirculation, frictional characteristics of blood cells on glass plates coated with DLC or MPC polymer are investigated with an inclined centrifuge microscope [2].

3.1. Introduction

Blood flow in microcirculation plays an important role in supplying tissues with nutrients and removing metastases. Extensive physiological research has been carried out to examine blood flow in microcirculation focusing on the complex interaction between blood cells, plasma proteins, and glycocalyx in the endothelial surface layer [10,11]. Numerical analysis has been performed for cell motion in a blood capillary considering the interaction between the cell and the endothelial surface layer [12], but there has been little experimental measurement data of friction characteristics to date. It is critically important to develop a method to measure this friction force acting on the blood cells moving along the vessel surface.

In recent years materials for coating implantable artificial organs or devices have attracted attention. Among them this paper deals with diamond-like carbon (DLC) film [13] and 2-methacryloyloxyethyl phosphorylcholine (MPC) polymer [14]. DLC is one of the carbon based coatings with amorphous structure which has properties similar to diamond. It has good resistance to corrosion and wear, low coefficient of friction, low partner aggressiveness, super flat smoothness, a thin film, and insulation properties. MPC was developed to create biomembrane structures artificially. It has a phosphorylcholine base that has a phospholipid polar group side chain, and has a characteristic to restrain proteinaceous absorption.

When the DLC or MPC polymer is coated on vascular devices, compatibility to blood is an important problem. The present paper focuses on friction characteristics of erythrocytes to these coating materials in a medium. The inclined centrifuge microscope is used first to observe the motion of erythrocytes moving on flat glass plates with and without coating of DLC or MPC polymer in a medium of plasma or saline under the effect of centrifugal force at an angle with respect to the plate. Friction characteristics of erythrocytes to these materials are then measured and compared with each other to characterize DLC and MPC polymer as a coating material from the viewpoint of the friction property of erythrocytes.

3.2. Experimental apparatus and principle

Inclined centrifuge microscope

A schematic diagram and specifications of the inclined centrifuge microscope system are shown in Fig. 10 and Table 2, respectively. In order to improve measurement performance, several components of the original equipment (Hayase et al., 2002) have been replaced in the present system. A pair of inclined containers of inner dimension of 10 mm × 8 mm × 1 mm (width × length × height) is mounted on the rotor of the centrifuge (KUBOTA, Model 1120). One of the two containers is filled with a medium containing blood cells and the other container remains empty. The rotation speed of the rotor is measured using a digital tachometer (ONO SOKKI, TM-2110, error: 0.02%). A reference signal of rotation, which is generated by a laser diode (NEO ARK, LDP-6930C) and a detector (NEO ARK, RD-102), and is delayed through a pulse generator (Hewlett Packard, HP81101A, 50 MHz) and a signal synthesizer (NF Circuit Design Block, WF1944), triggers a YAG (yttrium aluminum garnet) laser (KANOMAX, SPIV-30-20-ATT, 3 ns/pulse, 30mJ/pulse) and a CCD camera (Ikegami, SKC-141, 15 fps, 145 Mpixels). The exposure time of the CCD camera is fixed at 1/8000 s and the exposure timing is controlled to accurately synchronize with the rotation. The laser beam, which is guided through an optical fiber (NIKON, GFLG-5), illuminates the container for a very short interval of 3 ns during the exposure time of the CCD camera at the same angular position of the spinning rotor so that a still image of the plate can be observed. Erythrocytes moving on the plate are observed through a microscope (NIKON, CM-10) with objectives (Olympus, Cplan F1 10× and CF Plan EPI SLWD 50×), the light axis of which is adjusted normal to the plate at an angle of θ from the horizontal plane. The microscope was remodeled to change the optical axis 90 degrees by mirroring at the connecting point of the objective lens. The images are sent to a PC and stored on its hard drive.

In each measurement, 100 sequential images with an interval of the smallest multiple of the rotation period larger than 1/15 s were obtained. Each image was digitized into 1392 × 1024 pixels with a 256-level monochrome gradation and a diameter of 0.65 μm/pixel for the 10× objective lens. Fluctuation of the images due to inevitable error in synchronization was

Table 2. Specifications of inclined centrifuge microscope.

Angle of microscope	θ_0	0-50 deg
Angle of base plate	θ	40-90 deg
Angular frequency	ω	0-1257 rad/s
Magnification on 17inch monitor (10× and 50× objective lens)		×255, ×1275
Rotation radius	r_0	5.43×10^{-2} m
Rotation speed	N	0-12000 rpm

removed by translating the images based on grid lines of 5 μm in width etched on the back of the plates. The image data was processed by the PTV software program (Nexus, PIV Expert 2000) to obtain the velocity vectors of the erythrocytes. After the removal of background noise and smoothing, centers of gravity of all erythrocytes were obtained. The particle tracing velocimetry method was then applied in order to determine the velocity vectors of all the cells based on the distribution of cell centers at two time instants. The cell velocity is evaluated by the velocity component parallel to the tangential force since the rotational velocity component is strongly affected by the fluctuation in synchronization.

Principle of friction force measurement

The plate is placed at the bottom of the container, which is inclined at an angle of θ from the horizontal plane. The container is filled with a medium (plasma or saline) in which erythrocytes have been dispersed. By applying rotation at an angular velocity ω the cells move in a radial direction under the effect of centrifugal force F, described as,

$$F = (\rho_r - \rho_m) V_r r_0 \omega^2, \tag{6}$$

where ρ_r, ρ_m are the density of the erythrocyte and the medium, respectively, V_r is the volume of the cell (Table 3), and r_0 is the rotation radius (Table 2). Note that we consider the case in which the effect of gravitation is negligible and the rotation radius is

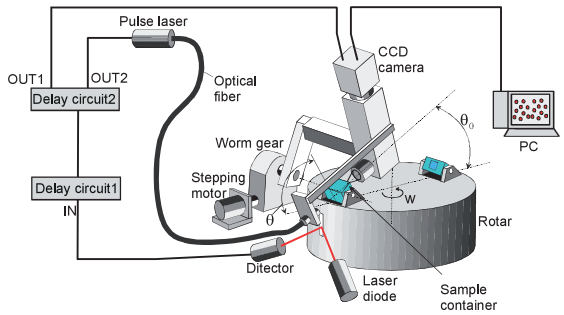

Fig. 10. Schematic of the inclined centrifuge microscope system.

Table 3. Physical properties of specimen.

Erythrocytes	
Diameter d_r	8.4×10^{-6} m
Height h_r	2.4×10^{-6} m
Volume V_r	8.7×10^{-17} m^3
Density ρ_r	1087 kg/m^3
Plasma	
Density ρ_p	1025 kg/m^3
Viscosity μ_p	1.2×10^{-3} Pa·s
Saline	
Density ρ_s	998.2 kg/m^3
Viscosity μ_s	1.01×10^{-3} Pa·s

assumed to be constant. After the cells contact the plate, the centrifugal force on each cell is naturally divided into two components; the normal force F_N and the tangential force F_T as,

$$F_N = F\sin\theta, \quad F_T = F\cos\theta. \tag{7}$$

The normal force F_N balances the reaction from the plate, and the tangential force F_T accelerates the cell along the plate. When the cell velocity U reaches a steady value, the tangential force F_T is equal to the sum of the friction force F_T* from the plate and the drag force f_D from the medium above the cell as

$$F_T = F_T^* + f_D. \tag{8}$$

Precisely modeling the drag force for the shape of an actual erythrocyte is difficult. Since the Reynolds number based on the diameter and velocity of the cell and on the kinematic viscosity of the medium is less than 10^{-3} for the condition examined in the present study, we use the drag coefficient C_D of the Stokes equation for a sphere,

$$f_D = C_D(h_r d_r)\frac{1}{2}\rho U^2, \quad C_D = 24/R_e \tag{9}$$

where h_r and d_r denote the height and the diameter of the erythrocyte, respectively (Table 3).

As the force components F_N and F_T are specified arbitrarily by adjusting the angle of the container θ and the angular velocity ω, measuring the cell velocity U for a variety of force conditions gives the friction characteristics of the erythrocytes moving along the plate. A finite time is required before the cells attain a steady velocity with all forces in equilibrium.

By the assumption that the friction force is approximately described as the viscous friction of the uniform shear flow between the cell and the plate, we have the following equation:

$$F_T^* = \mu\cdot\dot{\gamma}\cdot\pi d_r^2/4, \tag{10}$$

where $\dot{\gamma}$ is the equivalent shear rate of the flow in a gap between the cell and the plate. The equivalent gap width h_g is given as,

$$h_g = U / \dot{\gamma} . \quad (11)$$

3.3. Materials and methods

Human venous blood was sampled to a vacuum blood-collecting vessel (NIPRO NEO TUBE PET) from an informed healthy male volunteer of 24 years old. The blood anticoagulated by citric acid sodium (3.13 %) was centrifuged (1,000 g, 10 min) to separate plasma and erythrocytes. The plasma was centrifuged again in the same manner to purify it. A separate plasma and saline were then prepared as two mediums. Separated erythrocytes were distributed in the mediums at a volumetric concentration of 0.01%. The PH of the sample was 7.5±0.1. The experiment was performed within 6 hours after blood sampling and at a constant room temperature of 20±1 degrees Celsius. The physical properties of the materials are summarized in Table 3. The density of erythrocytes and that of the plasma are referred from our former study [2], whereas the other properties were obtained from the literature [2].

Pieces of cover glass made of synthetic quartz (Takahashi Giken Glass, 0.15 mm thickness) were used as the plates. Some of them were coated with DLC or MPC polymer. DLC coating was fabricated by chemical vapor deposition (CVD) technique. The deposition was performed for 20 minutes under the condition of 2.2×10^{-2} torr and -700 V of substrate selfbias voltage. A methane gas was used as a precursor gas. MPC polymer was coated on a different plate by putting the plate into PMB ethanol solution (0.2 wt%) and drying it naturally. The PMB ethanol is a mixture of non-water-soluble PMB30 and water-soluble PMB80 in a ratio of 9:1.

Figure 11 shows photographs of (a) a glass plate coated with MPC polymer (MPC-coated plate), (b) a glass plate coated with DLC (DLC-coated plate), and (c) a glass plate without coating (non-coated plate), respectively. The MPC-coated plates look the same as the non-coated plates. The DLC-coated plates are colored light brown but transparent.

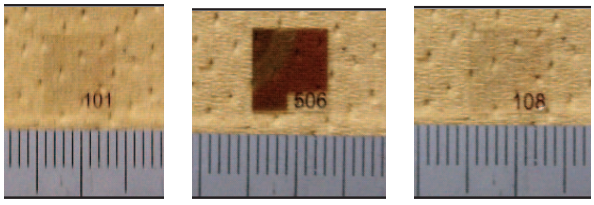

(a) (b) (c)

Fig. 11. Sample plates (small division = 1 mm): (a) MPC-coated plate, (b) DLC-coated plate, (d) non-coated plate.

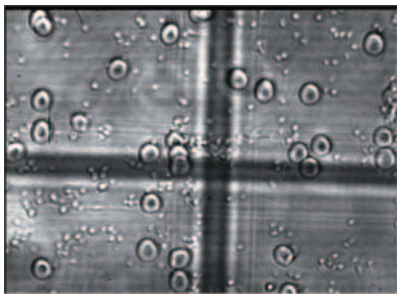

Fig. 12. Behavior of erythrocytes in plasma on MPC-coated plate (F_T = 35 pN, F_N = 47 pN).

3.4. Results

The motion of the erythrocytes on the three kinds of plates was first observed by using the 50× objective lens of the inclined centrifuge microscope. The friction characteristics were then measured by the 10× objective lens. In the experiment, tangential force component F_T was set between 2.5 pN and 40 pN while maintaining the normal force component F_N at 47 pN.

Figure 12 shows a snapshot of a motion picture in which erythrocytes (large circles) are moving upward in the figure on the MPC-coated plate in the medium of plasma under the effect of centrifugal force with a tangential force component F_T of 35 pN and a normal force component of F_N of 47 pN. As mentioned above the tangential force component drives the cells to move on the plate and the normal force component pushes the cells on the plate. In the figure, the configurations of erythrocytes are clearly defined including a dark part in the center corresponding to a typical concave shape. The small dots in the figure are most likely aggregations of fibrinogen in plasma. Similar results were obtained for the non-coated plate and the DLC-coated plate under the same conditions.

Next we measured the velocities of the cells to evaluate the friction characteristics of erythrocytes on the plates. In order to observe a sufficient number of cells we used the 10× objective lens. The normal force was fixed at F_N = 47 pN and the tangential force F_T was set at 5 pN intervals between 5 and 40 pN using plasma as a medium on the MPC-coated, DLC-coated, and non-coated plates, and at F_T = 2.5, 5, 10, 20, 30 pN using saline as a medium on the MPC-coated plate.

100 sequentially captured images were processed by the PTV software to obtain the velocities of cells using two sequential images. The typical number of velocities of cells obtained on the image was 140 in the present work.

By introducing the results into Eq. (8), we obtained the friction force working between the cells and the plate. Equivalent shear rate and gap width were obtained from Eqs. (10) and (11). Figure 13(a) shows the friction force and the equivalent shear rate as a function of the mean cell velocity for the MPC-coated,

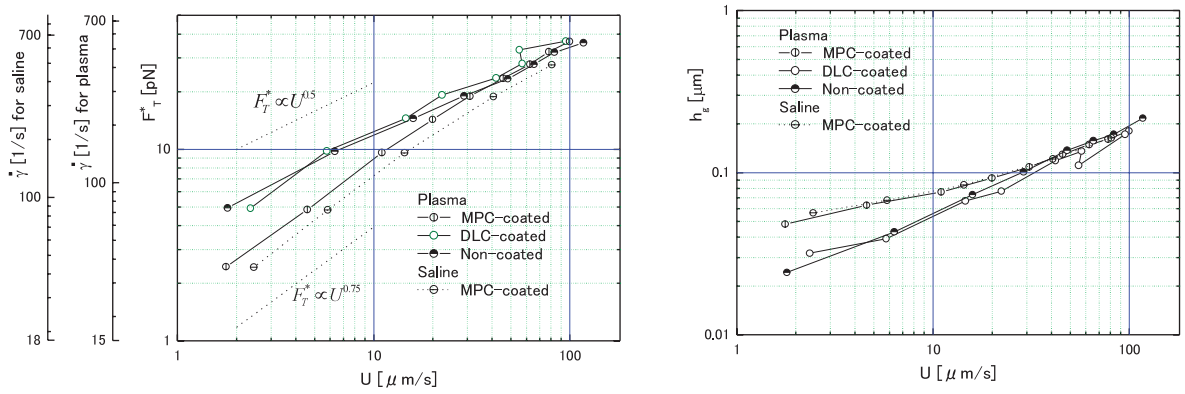

(a) (b)

Fig. 13. Friction characteristics of erythrocytes: (a) friction and equivalent shear rate and (b) equivalent gap width.

DLC-coated, and non-coated plates in plasma and the MPC-coated plate in saline. Figure 13 (b) shows the corresponding results for the equivalent gap width.

3.5. Discussion

The friction characteristics of erythrocytes in plasma using the DLC-coated and non-coated plates are similar changing approximately proportional to the 0.5th power of the cell velocity. The cells stick to the plates when plasma is replaced with saline, implying that plasma protein plays an important role to determine friction characteristics. The results of the MPC-coated plate using plasma are similar to those using the other plates in the range of relatively large cell velocity, but deviate from those with decreased cell velocity. The results change nearly proportional to the 0.75th power of the cell velocity in the range of small velocities less than 10 μm/s. The friction force observed in the MPC-coated plate in saline is similar to that in plasma but somewhat smaller. This means the friction characteristics of cells using the MPC-coated plate is essentially independent of plasma protein. Therefore, in the range of large cell velocities, in which all the friction characteristics are similar, plasma protein plays a secondary role in determining friction characteristics.

Shear stress in the fluid flow between the cell and the plate should play the essential role to determine the friction force. The cell velocity, the gap width between the cell and the plate, and the viscosity of the fluid are the factors which determine the flow shear stress. The shear rate in the gap ranged between 30 1/s and 700 1/s in a present experiment. It should be noted that the resultant shear force acted only on the bottom surface of the cell to counterbalance the centrifugal force. Therefore, the effect of this shear rate on the cell motion is different from that on a cell in a uniform shear flow. The equivalent gap distance between the cell and the plate ranged between 0.02 μm and 0.2 μm. The results for the MPC-coated plates with plasma and saline were identical. The gap widths for the DLC-coated and non-coated plates were almost the same and were smaller than those of MPC-coated plates. In a previous study [2], we proposed that the distance corresponds to the size of plasma protein, but the present result for the MPC-coated plate with saline invalidates this possibility. Electro-chemical force, such as the strong attraction of water molecules on the surface of MPC polymer [14], or hydrodynamic force, such as squeezing force due to the movement of the cell, should be considered to determine the distance, but these considerations go beyond the scope of the present study. The deviation of the friction force and the equivalent gap width of the DLC-coated and non-coated plates from that of the MPC-coated plate in small velocities is probably explained by the effect of additional friction force due to plasma proteins.

4. Conclusions

The author's group is doing research to analyze complex blood flows by numerical simulation, experimental measurement, and their coupled method. The coupled method enables us to perform a highly accurate and high speed analysis of the local and fine structure of complex blood flows.

References

[1] Funamoto K, Hayase T, Saijo Y, and Yambe T. Numerical Experiment of Transient and Steady Characteristics of Ultrasonic-Measurement- Integrated Simulation in Three-Dimensional Blood Flow Analysis. *Ann Biomed Eng* **37**, 34-49, 2008.

[2] Kandori T, Hayase T, Inoue K, Funamoto K, Takeno T, Ohta M, Takeda M, and Shirai A. Frictional Characteristics of Erythrocytes on Coated Glass Plates Subject to Inclined Centrifugal Forces. *J Biomech Eng, Trans ASME* **190**, 051007-1-8, 2008.

[3] Caro CG, Fitzgera J, and Schroter RC. Atheroma and arterial wall shear - observation, correlation and proposal of a shear dependent mass transfer mechanism for altherogenesis. *Proc R Soc Lond* B Biol Sci **177**, 109-159, 1971.

[4] Depaola N, Gimbrone MA, Davies PF, and Dewey CF. Vascular endothelium responds to fluid shear-stress gradients. *Arterioscler Thromb* **12**, 1254-1257, 1992.
[5] Li Z and Kleinstreuer C. A new wall stress equation for aneurysm-rupture prediction. *Ann Biomed Eng* **33**, 209-213, 2005.
[6] Funamoto K, Hayase T, Shirai A, Saijo Y, and Yambe T. Fundamental study of ultrasonic-measurement-integrated simulation of real blood flow in the aorta. *Ann Biomed Eng* **33**, 415-428, 2005.
[7] Funamoto K, Hayase T, Saijo Y, and Yambe T. Numerical study on variation of feedback methods in ultrasonic-measurement-integrated simulation of blood flow in the aneurysmal aorta. *JSME Int J* Ser C 49, 144-155, 2006.
[8] Patankar SV. *Numerical heat transfer and fluid flow.* Hemisphere Pub. Corp., Washington DC/New York, 1980.
[9] Hayase T, Humphrey JAC, and Greif R. A consistently formulated quick scheme for fast and stable convergence using finite-volume iterative calculation procedures. *J Comput Phys* **98**, 108-118, 1992.
[10]Schmid-Schoenbein GW. Biomechanics of microcirculatory blood perfusion. *Annual Review of Biomedical Engineering* **1**, 103-127,1999.
[11]Pries AR, Secomb TW, and Gaehtgens P. The endothelial surface layer. *European Journal of Physiology* **440**, 653-666, 2000.
[12]Secomb TW, Hsu R, and Pries AR. A model for red blood cell motion in glycocalyx-lined capillaries. *American Journal of Physiology* (Heart and Circulatory Physiology 43) **274**, H1016-H1022, 1998.
[13]Mohanty M, Anilkumar TV, Mohanan PV, Muraleedharan CV, Bhuvaneshwar GS, Derangere F, Sampeur Y, and Suryanarayanan R. Long term tissue response to titanium coated with diamond like carbon. *Biomolecular Engineering* **19**, 125-128, 2002.
[14]Ishihara K, Nomura H, Mihara T, Kurita K, Iwasaki Y, and Nakabayashi N. Why do phospholipid polymers reduce protein adsorption? *J Biomedical Materials Research* **39**, 323-330, 1998.